Inherent stress correlations in a quiescent two-dimensional liquid: Static analysis including finite-size effects

Anaël Lemaître
Laboratoire Navier, UMR 8205, École des Ponts, IFSTTAR, CNRS, UPE, Champs-sur-Marne, France
(Received 3 April 2017; revised manuscript received 17 August 2017; published 1 November 2017)

After constructing a formalism to analyze spatial stress correlations in two-dimensional equilibrated liquids, we show that the sole conjunction of mechanical balance and material isotropy demands all anisotropic components of the inherent state (IS) stress autocorrelation matrix to decay at long range as $1/r^2$ in the large system size limit. Furthermore, analyzing numerical simulation data for an equilibrated supercooled liquid, we bring evidence that, in finite-sized periodic systems, the autocorrelations of pressure and shear stresses present uniform backgrounds of amplitudes proportional to the inverse cell area. These backgrounds bring relevant contributions to macroscopic IS stress fluctuations, with the consequence that the latter scale as inverse area, yet in an anomalous way, inconsistent with viewing an IS as equivalent, in the thermodynamic limit, to an ensemble of independent finite-sized subsystems. In that sense, ISs are not spatially ergodic.

DOI: 10.1103/PhysRevE.96.052101

I. INTRODUCTION

At low temperature, equilibrated supercooled liquids evolve via rare transitions between the basins of attraction of inherent states [(ISs), i.e., local minima of the potential energy surface] around which they are most of the time just vibrating [1,2]. Inherent states, hence, largely determine the thermodynamic, dynamic, and transport properties of supercooled liquids [3–6] and are also the glassy solids formed when a liquid is quenched well below the glass transition. A detailed knowledge of their properties is thus crucial to these various topics.

On this matter, it was recently found, in both two- and three-dimensional (3D) numerical models of equilibrated supercooled liquids [7,8], that ISs carry long-range anisotropic stress correlations of a form similar to elastic Green's functions. This finding raises many questions, for example, about how the thermodynamic limit is reached in the presence of such long-ranged correlations, or about their role in the relaxation process, e.g., by inducing correlations between relaxation events [7]. In one instance, the impact of stress correlations on macroscopic properties is already documented as they were found to induce similar long-range correlations of the local elasticity tensor [9], and thus to enhance sound damping in glasses, in a manner that agrees with experimental data [10–13].

Basic questions, however, remain about the origin and structure of IS stress correlations. They can be viewed as resulting from the accumulation of relaxation events akin to Eshelby transformations, i.e., local rearrangements that imprint long-range elastic deformations in the surrounding amorphous medium [7,14], an effect observed in quiescent colloidal formers [15,16]. Yet, similar stress correlations were also found in granular systems close to jamming, i.e., in near the point where elasticity breaks down [17]. It is thus unclear under which general conditions long-range stress correlations exist, or why the amplitudes of certain components of the IS stress autocorrelation matrix were systematically found to be in simple ratios [7,8]. Besides, the analysis of these correlations faces significant technical hurdles arising from the tensorial character of stress: Stress anisotropies, which exist both in ISs and parent liquid configurations [7,18,19], were initially believed to be a hallmark of elasticity, and later understood to be an artifact of the representation of stress in a unique reference frame [8,20].

In this paper, with a view to preparing future studies of both relaxation in supercooled liquids and sound damping in glasses, we focus on the static autocorrelation of IS stress, and provide a step-by-step account of how it is measured and analyzed in two dimensions using a formalism that extends and adapts a previous study of 3D systems [8].

Three main results will emerge from our analysis. First, it will appear that the sole conjunction of mechanical balance and material isotropy constrains so tightly the overall structure of the whole autocorrelation matrix that it is entirely fixed, in the infinite medium limit, by the pressure autocorrelation only. It will follow, as a corollary, that all anisotropic correlation components decay at large distance as $1/r^2$.

Second, using a 2D numerical model of equilibrated liquid, we will evidence that the Fourier components of the IS stress autocorrelation matrix are completely devoid of finite-size deviations in periodic cells. This empirical finding will allow us to write, for the real-space autocorrelation, a general expression valid in sufficiently large (well beyond the atomic scale) but finite-sized periodic systems. The autocorrelation field will appear to be the sum of: its infinite medium limit value; the trivial superposition of periodic images; and a uniform background of amplitude proportional to the inverse system area.

Third, we will use this general expression to decompose macroscopic stress fluctuations into microscopic contributions associated with distinct features of the autocorrelation matrix. The long-range anisotropic correlations will appear irrelevant by reasons of symmetry, and only two terms will contribute: one originating from local stress inhomogeneities; the other, from the autocorrelation backgrounds. This second term, while respecting the inverse area scaling, causes macroscopic stress fluctuations to take values that are incompatible with viewing a large IS as statistically equivalent to a set of independent finite-sized subsystems. We will refer to this nonequivalence by saying that ISs are not spatially ergodic.

Our paper is organized as follows. Section II expounds how IS stress fields are computed either via coarse graining or in Fourier space. Sections III and IV present our formalism along with data analysis in, respectively, real and Fourier space. Our main results are reached in Sec. V, where we derive a general expression for the real-space autocorrelation in an infinite medium, and in Sec. VI, where we study finite-size effects.

II. INHERENT STRESS FIELD

The Fourier coefficients of a $L \times L$-periodic scalar field $f(\underline{r})$ are defined as:

$$\hat{f}_{\underline{k}} = \int_A d\underline{r}\, f(\underline{r})\, e^{-i\underline{k}\cdot\underline{r}} \tag{1}$$

with $A = L^2$ the area. They take values on the discrete reciprocal space, $\underline{k} = \frac{2\pi}{L}\,\underline{n}$ with $\underline{n} \in \mathbb{Z}^2$. The inverse transformation is

$$f(\underline{r}) = \frac{1}{A} \sum_{\underline{k}} e^{i\underline{k}\cdot\underline{r}}\, \hat{f}_{\underline{k}}, \tag{2}$$

where the sum runs over the reciprocal space. In some cases, our argument will involve nonperiodic functions $f(\underline{r})$ defined on the infinite plane; their Fourier transforms are defined just as in (1), but will be denoted $\hat{f}(\underline{k})$ to emphasize that they take values on the $\underline{k}$ continuum; the inverse transform then reads:

$$f(\underline{r}) = \frac{1}{(2\pi)^2} \int d\underline{k}\, e^{i\underline{k}\cdot\underline{r}}\, \hat{f}(\underline{k}). \tag{3}$$

A. Coarse graining

1. Method

Local stress is measured using the method proposed by Goldhirsch and Goldenberg, which proceeds by identification of the fluxes appearing in conservation equations [21] after microscopic density is defined as $\rho(\underline{r}) = \sum_i \phi(\underline{r} - \underline{r}_i)$, with ϕ is a coarse-graining function that is positive and isotropic, vanishes beyond a cutoff r_c, and integrates to unity. In inherent states, local stress is found to read:

$$\sigma_{\alpha\beta}(\underline{r}) = \frac{1}{2} \sum_{i,j;i\neq j} F_{ij}^{\alpha} r_{ij}^{\beta} \int_0^1 ds\, \phi(\underline{r} - \underline{r}_i - s\underline{r}_{ij}) \tag{4}$$

with $\underline{r}_i$ the position of particle i, $\underline{r}_{ij} \equiv \underline{r}_j - \underline{r}_i$ (modulo cell periodicity), and $\underline{F}_{ij} = [V'_{ij}(r_{ij})/r_{ij}]\,\underline{r}_{ij}$ the force exerted by j on i, which derives from the pair potential V_{ij}. The symmetry of stress is guaranteed by $\underline{F}_{ij}\ \underline{r}_{ij} = \underline{r}_{ij}\ \underline{F}_{ij}$ (juxtaposition denotes tensor products).

In Fourier space, Eq. (4) becomes: $\widehat{\underline{\underline{\sigma}}}_{\underline{k}} = \widehat{\phi}(\underline{k})\, \widehat{\underline{\underline{\sigma}}}^{\delta}_{\underline{k}}$, with

$$\widehat{\sigma}^{\delta}_{\alpha\beta\,\underline{k}} = \frac{1}{2} \sum_{i,j;i\neq j} F_{ij}^{\alpha} r_{ij}^{\beta}\, \frac{e^{-i\underline{k}\cdot\underline{r}_i} - e^{-i\underline{k}\cdot\underline{r}_j}}{i\underline{k}\cdot\underline{r}_{ij}} \tag{5}$$

showing that the Goldhirsch-Goldenberg local stress is just a convolution by ϕ of the microscopic stress $\underline{\underline{\sigma}}^{\delta}$ [22]. The δ indicates that $\underline{\underline{\sigma}}^{\delta}$ is the stress in the limit when ϕ is the 2D Dirac delta function. The coarse-grained field $\underline{\underline{\sigma}}$ is thus expected to carry the same long-range correlations as $\underline{\underline{\sigma}}^{\delta}$, but to present some blurring at small scales.

2. Two essential properties

Stipulating that ϕ integrates to unity guarantees a crucial consistency requirement: the space average of the local stress field $\frac{1}{A}\int \underline{\underline{\sigma}}(\underline{r}) = \overline{\underline{\underline{\sigma}}}$ the Irvin-Kirkwood macroscopic stress, which is defined as:

$$\overline{\sigma}_{\alpha\beta} = \frac{1}{2\,A} \sum_{i,j;i\neq j} F_{ij}^{\alpha} r_{ij}^{\beta}. \tag{6}$$

Inherent states being mechanically stable, one expects their local stress fields to be divergence free. It is instructive to check that this property is indeed satisfied. To do so, we write $i\underline{k}\cdot\widehat{\underline{\underline{\sigma}}}_{\underline{k}} = i\widehat{\phi}(\underline{k})\,\underline{k}\cdot\widehat{\underline{\underline{\sigma}}}^{\delta}_{\underline{k}}$ and find:

$$\begin{aligned} i\underline{k}\cdot\widehat{\underline{\underline{\sigma}}}^{\delta}_{\underline{k}} &= \frac{1}{2} \sum_{i,j;i\neq j} \underline{F}_{ij}(e^{-i\underline{k}\cdot\underline{r}_i} - e^{-i\underline{k}\cdot\underline{r}_j}) \\ &= \sum_i e^{-i\underline{k}\cdot\underline{r}_i}\, \underline{F}_i, \end{aligned} \tag{7}$$

where $\underline{F}_i = \sum_{j\neq i} \underline{F}_{ij}$ is the total force applied by the system on atom i. Quite consistently, local stress is strictly divergence free in ISs because of mechanical balance at atom scale, i.e., the vanishing of all $\underline{F}_i$'s.

3. Technicalities

The simulation data used in this work were obtained from equilibrated configurations of the same binary Lennard-Jones (LJ) mixture as in previous studies [7,14]. All quantities are given in LJ units. Only one temperature was used, $T = 0.28$, for which the relaxation time of shear stress is about 2000. ISs are computed using the fast inertial relaxation engine (FIRE) algorithm [23] with a precision 10^{-10}, defined as the maximum acceptable value of any component of the residual atomic force.

In practice, the stress field is sampled on a grid in either real or Fourier space and computed using the corresponding expression, Eq. (4) or Eq. (5). Using either computation method may entail very different numerical costs. Suppose indeed that, in dimension d, we seek to compute stress in an L^d system for a fixed spatial discretization Δ: either in real or Fourier space, we need to evaluate $(L/\Delta)^d$ points. In expression (4), the stress at any point $\underline{r}$ only depends on the contribution of pairs of atoms that lie withing the range r_c; it can hence be computed using Verlet lists in an L-independent number of operations. So the complete calculation of a stress field using the Goldhirsch-Goldenberg coarse graining can be performed using $\propto L^d$ operations. In contrast, computing stress in Fourier space, using Eq. (5), requires, for every $\underline{k}$, to add the contributions of all atoms in the system, i.e., to perform a number of operations that scales as L^d. In total, a complete stress field evaluation thus requires $\propto L^{2d}$ operations.

This difference in computational costs is a minor issue for small systems, but becomes determining for large ones. For example, on a given AMD Opteron computer, it takes about 10 s to compute a stress field using the real-space expression (4) for our largest systems (45395 atoms), at a resolution $\Delta = 0.5a$, with a the large atoms' size. On the same computer, at the same resolution, the Fourier calculation takes over 4 h [24]. Such a duration is impracticable since, to gain accuracy

about long-range correlations, we need to accumulate data from $\simeq$50000 ISs in a given equilibrium ensemble.

Computing stress via coarse graining, hence is the only usable method for very large systems, yet has the drawback that local stress, as defined by Eq. (4), is nonzero only within the distance r_c from the segments joining atoms in interaction. If r_c is much smaller than the typical interatomic distance, sampling stress on a grid of fixed spatial step Δ may not provide statistically meaningful data because too many grid points only carry zero values. For this reason, the real-space expression must be used with r_c large enough that most points $\sigma_{\alpha\beta}(\underline{r})$ capture the contribution of at least one neighboring pair, which necessarily introduces some blurring at short distance, and modifies the shape of stress correlations at short range. We will show, however, that it does not affect long-range correlations and that relevant short-range correlations of stress can easily be accessed nevertheless. The effect of coarse graining on correlations will be addressed when necessary.

We use $\phi(\underline{r}) = \frac{15}{8\pi r_c^2}[1-(r/r_c)^4]^2$ for $r < r_c$, $\phi(\underline{r}) = 0$ otherwise. The real-space discretization step needs to be small enough to resolve short-range correlation peaks; $\Delta = 0.5a$, was found satisfactory. The smaller r_c, the faster the computation, and the better we avoid blurring. Yet, as we explained before, if r_c is too small, i.e., when ϕ is too close to a Dirac δ function, we risk losing accuracy due to poor sampling. The choice of r_c results from a balance between these constraints. We have tested different values ranging from 0.5–4 and observed they provided fully consistent results. If not explicitly stated, we use $r_c = 1$, which provides a fair compromise.

B. Stress decomposition and corresponding maps

Stress, being symmetric, has three independent components in two dimensions. The Cartesian components σ_{xx}, σ_{yy}, and σ_{xy} are a poor choice of representation because they do not reflect clearly how stress behaves under rotations. As in Ref. [7], we decompose stress as follows:

$$\begin{aligned}\sigma_1 &= -\tfrac{1}{2}(\sigma_{xx}+\sigma_{yy})\\ \sigma_2 &= \tfrac{1}{2}(\sigma_{xx}-\sigma_{yy})\\ \sigma_3 &= \sigma_{xy}.\end{aligned} \tag{8}$$

We will see later that this representation tremendously simplifies the analysis of stress correlations, especially in view of probing material isotropy. Of course, σ_1 is just pressure. The component σ_2 is the shear stress in a frame rotated by $\pi/4$, so it is expected to share, in an isotropic medium, the same statistical properties as σ_3 up to this rotation. These three components define a vector representation of stress denoted $\underset{\sim}{\sigma} \equiv (\sigma_1,\sigma_2,\sigma_3)$; the tilde is used to distinguish it from usual vectors.

Maps of $\sigma_1(\underline{r})$, $\sigma_2(\underline{r})$, and $\sigma_3(\underline{r})$, computed in a single inherent state of an $L = 80$ system (in equilibrium at $T = 0.28$), are displayed on Fig. 1. As noted in Ref. [7], while pressure does not display any hint of anisotropy, the deviatoric fields do present marked orientations: along diagonals for σ_3 and along the x and y axes for σ_2.

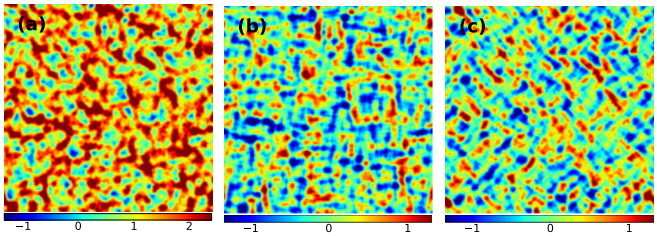

FIG. 1. Coarse-grained fields—pressure (a) σ_1, (b) σ_2, and (c) σ_3—measured in one IS of a $L = 80$ system equilibrated at $T = 0.28$, using $r_c = 2$ for better visibility.

III. STRESS AUTOCORRELATION IN REAL SPACE

A. Raw data analysis

Our study focuses on the IS stress autocorrelation matrix:

$$\underset{\approx}{C}(\underline{r}) \equiv \langle \underset{\sim}{\sigma}(\underline{r}_0+\underline{r};t)\,\underset{\sim}{\sigma}(\underline{r}_0;t)\rangle_c \tag{9}$$

with $\langle AB\rangle_c = \langle AB\rangle - \langle A\rangle\langle B\rangle$ the second cumulant. As juxtaposition denotes the tensor product, $\underset{\approx}{C}$ is the matrix with components $C_{ab} = \langle \sigma_a(\underline{r}_0+\underline{r};t)\,\sigma_b(\underline{r}_0;\overset{\approx}{t})\rangle_c$. It does not depend on time t, because our systems are equilibrated. Thanks to translation invariance, it does not depend on $\underline{r}_0$ either, hence is a function of $\underline{r}$ only, and also verifies $C_{ab}(\underline{r}) = C_{ba}(-\underline{r})$. Together with inversion symmetry, $C_{ab}(\underline{r}) = C_{ab}(-\underline{r})$, the latter relation guarantees matrix symmetry: $C_{ab} = C_{ba}$.

To provide a general overview of the spatial structure of these correlation fields, we display all of them (for $L = 160$ systems) on Fig. 2, as a matrix of pictures. Using translation invariance, we position the origin of coordinates at the center of each picture. The autocorrelation of σ_1 (pressure) shows a visible nonzero value only at the origin of space—a tiny white spot that manifests a sharp correlation peak. We will see later that σ_1 does not vanish away from the central peak, but decays toward a small but nonzero background value.

To the exception of the pressure autocorrelation, all the fields of Fig. 2 present long-range anisotropic tails. In particular, the autocorrelations of σ_2 and σ_3 display a clear $\pm\cos(4\theta)$ symmetry: σ_2 positively correlates along horizontal and vertical directions, while σ_3 positively correlates along diagonals. These features correspond to the anisotropies seen on the stress maps of Fig. 1. The complete set of correlation fields, however, also reveals anisotropic cross correlations between pressure and shear stresses, as well as between σ_2 and σ_3, with complex angular dependencies that could not be guessed by visual inspection of stress maps.

Close examination of these pictures shows that C_{22} and C_{33} present—like pressure—a positive central peak, a feature, however, absent on all cross correlations. To emphasize this point, we report on Fig. 3(a) various cuts along the lines of maximum intensity: for C_{22} and C_{33} along the x and $\theta = \pi/4$ axes; for C_{12} along x; and C_{13} along the $\theta = \pi/4$ axis (both cuts along negative lobes). Clearly, C_{22} and C_{33} present the same central peak of width of order $r_c = 1$, while C_{12} and C_{13} vanish at $r = 0$.

Away from the peak, the C_{22} and C_{33} cuts along either positive and negative lobes collapse. Moreover, the four cuts made through negative lobes (from C_{12}, C_{13}, as well as C_{22} and C_{33}) merge at long range showing that these cross

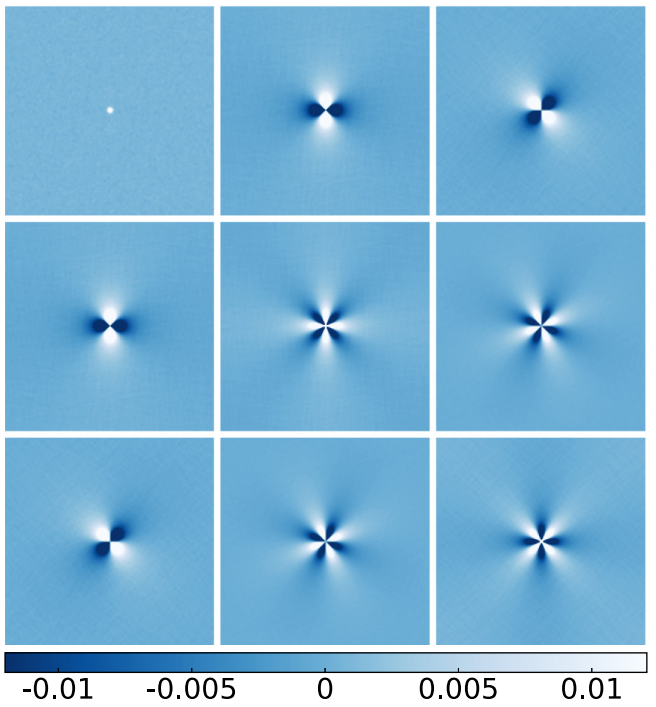

FIG. 2. The IS stress autocorrelation measured in $L = 160$ systems equilibrated at $T = 0.28$ and presented as a matrix of pictures corresponding to the fields C_{ab} with $a,b = 1 \ldots 3$. In each frame, the origin of space lies at the center. The matrix is clearly symmetric: $C_{ab} = C_{ba}$. Note that C_{11} resembles a δ function, and that C_{22} and C_{33} have opposite signs.

correlations and self-correlations have the same amplitude—a rather intriguing feature that will be explained at the end of Sec. V. The long-range decay of these correlations is further characterized by reporting the cuts of C_{22} and C_{33} in a log-log plot [Fig. 3(b)], which shows the $1/r^2$ decay (dashed line) to be very nicely satisfied. This analysis thus supports that beyond a central peak the autocorrelations C_{22} and C_{33} essentially match the $+\cos(4\theta)/r^2$ and $-\cos(4\theta)/r^2$ forms. We will see, however, that a more quantitative analysis shows evidence of slight, but important, departure from these expressions.

Let us close this section by examining the effect of coarse graining. Our above discussion used stress fields computed with $r_c = 1$. We expect that this parameters plays little role since varying it amounts to convolving the fields $\sigma_a^\delta(\underline{r})$ [defined by Eqs. (5) and (8)] with kernels of increasing width. This is verified on Fig. 3(c), where cuts of C_{33} along its positive, $\theta = \pi/4$, lobe are reported for three values of $r_c = 0.5$, 1, and 2. As expected, the width of the central peak grows with r_c, while the long-range correlation tails are essentially cutoff independent.

B. Radial form

In Ref. [8] we showed that stress anisotropies are a consequence of material isotropy. Here, we adapt to the 2D case the formalism presented then, which is based on accessing stress correlation in radial frames.

The reference Cartesian (lab) frame is denoted $\mathcal{F} = (\underline{e}_x, \underline{e}_y)$. For any vector $\underline{r}$, we define $\hat{\underline{r}} \equiv \underline{r}/r$ and introduce

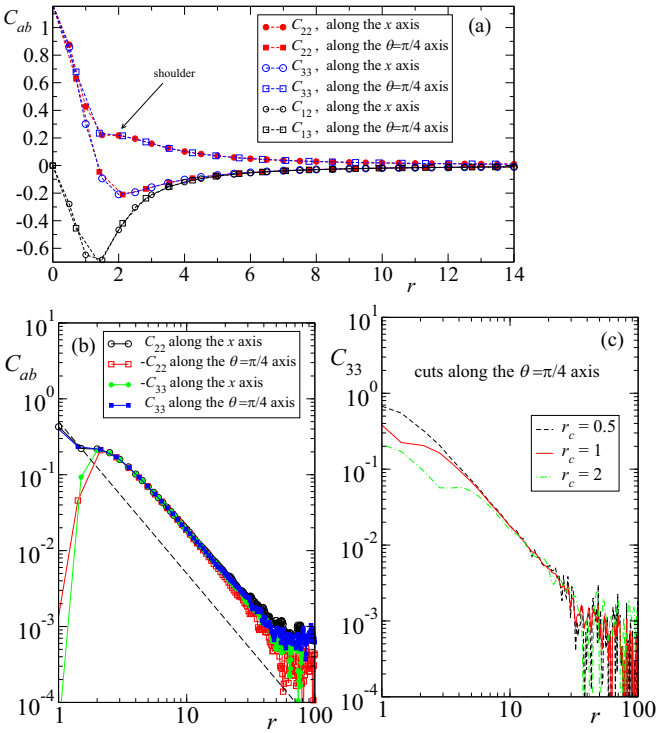

FIG. 3. Cuts of the spatial autocorrelation functions from Fig. 2 ($L = 160$, $T = 0.28$) along the x and the $\theta = \pi/4$ axes. (a) Comparing C_{22} and C_{33} along both axes with C_{12} along x and C_{13} along $\theta = \pi/4$: the central peak is displayed by the self-correlations (C_{22} and C_{33}) but not by the cross correlations (C_{12} and C_{13}); its width $\simeq 1.5$ compares with the coarse-graining radius $r_c = 1$. (b) log-log plots of C_{22} and C_{33} cuts modulo a minus sign to make the tail data positive; the dashed line is $\propto 1/r^2$. (c) C_{33}, $\theta = \pi/4$ cuts obtained with different values of the coarse-graining radius r_c: the peak width grows with r_c, but the tail is unchanged.

the frame $\mathcal{F}^{\hat{r}} \equiv (\underline{e}_r, \underline{e}_\theta)$, with

$$\underline{e}_r \equiv \hat{\underline{r}} = \begin{vmatrix} \cos\theta \\ \sin\theta \end{vmatrix} \quad \underline{e}_\theta = \begin{vmatrix} -\sin\theta \\ \cos\theta \end{vmatrix}. \tag{10}$$

By extension of the terminology used for 3D tensors, we call spherical components the coordinates of stress such as defined in (8). More specifically:

(i) we call Cartesian spherical (CS), the vector $\underset{\sim}{\sigma}$ as defined in (8), i.e., using the matrix components of $\underline{\underline{\sigma}}$ in the reference frame $\mathcal{F}$;

(ii) we call radial spherical (RS) and denote $\underset{\sim}{\sigma}^{\hat{r}}$ the spherical vector representation based on the matrix expression of stress in some arbitrary frame $\mathcal{F}^{\hat{r}}$, i.e., with components:

$$\begin{aligned} \sigma_1^{\hat{r}} &= -\tfrac{1}{2}(\sigma_{rr} + \sigma_{\theta\theta}) \\ \sigma_2^{\hat{r}} &= \tfrac{1}{2}(\sigma_{rr} - \sigma_{\theta\theta}) \\ \sigma_3^{\hat{r}} &= \sigma_{r\theta}. \end{aligned} \tag{11}$$

The great interest of using these spherical components is that $\underset{\sim}{\sigma}$ and $\underset{\sim}{\sigma}^{\hat{r}}$ are related by a very simple expression:

$$\underset{\sim}{\sigma}^{\hat{r}} = \mathcal{D}^{\hat{r}} \cdot \underset{\sim}{\sigma} \tag{12}$$

with

$$\mathcal{D}^{\hat{r}} = \begin{pmatrix} 1 & 0 & 0 \\ 0 & \cos 2\theta & \sin 2\theta \\ 0 & -\sin 2\theta & \cos 2\theta \end{pmatrix}, \tag{13}$$

which is a rotation matrix, since $(\mathcal{D}^{\hat{r}})^T$ is its inverse. It is immediately obvious from this expression that a $\pi/4$ rotation of the frame swaps the values of σ_2 and σ_3, which is the basis of our previous comment that the CS fields $\sigma_2(\underline{r})$ and $\sigma_3(\underline{r})$ are expected to be essentially equivalent up to this rotation.

The RS stress autocorrelation field is defined as:

$$\overset{\circ}{\underset{\approx}{C}}(\underline{r}) = \langle \underset{\sim}{\sigma}^{\hat{r}}(\underline{r}_0 + \underline{r})\, \underset{\sim}{\sigma}^{\hat{r}}(\underline{r}_0)\rangle_c. \tag{14}$$

For any pair of points, $\underline{r}_0$ and $\underline{r}_0 + \underline{r}$, it is the correlation matrix between the stress components in frame $\mathcal{F}^{\hat{r}}$. It is clearly independent of $\underline{r}_0$, thanks to translation invariance, and like $\underset{\approx}{C}$ is a symmetric matrix of centrosymmetric fields. Using Eq. (12), it reads:

$$\overset{\circ}{\underset{\approx}{C}}(\underline{r}) = \mathcal{D}^{\hat{r}} \cdot \underset{\approx}{C}(\underline{r}) \cdot (\mathcal{D}^{\hat{r}})^T. \tag{15}$$

C. Case of isotropic media

A key element in our argument is that the RS autocorrelation [Eq. (14)] is $\hat{r}$ independent in an isotropic medium. It is then a function of distance r only, and can be denoted $\overset{\circ}{\underset{\approx}{C}}(r)$ with the consequence that the CS autocorrelation,

$$\underset{\approx}{C}(\underline{r}) = (\mathcal{D}^{\hat{r}})^T \cdot \overset{\circ}{\underset{\approx}{C}}(r) \cdot \mathcal{D}^{\hat{r}} \tag{16}$$

is angle dependent. We will later show that this relation accounts for the anisotropies seen in Fig. 2.

Isotropy has another important implication. In three dimensions, we found that invariance under axial rotations about an arbitrary $\hat{r}$ strongly constrains the form of correlation fields [8]. This invariance also applies in two dimensions: indeed, considering the plane as embedded in the 3D space, the axial rotation about $\hat{r}$ by π maps the plane onto itself; it reduces there to mirror symmetry and transforms $(\underline{e}_r, \underline{e}_\theta)$ into $(\underline{e}_r, -\underline{e}_\theta)$, and $\underset{\sim}{\sigma}$ into $\mathcal{D}_M \cdot \underset{\sim}{\sigma}$, with:

$$\mathcal{D}_M = \begin{pmatrix} 1 & 0 & 0 \\ 0 & 1 & 0 \\ 0 & 0 & -1 \end{pmatrix}. \tag{17}$$

In an isotropic problem, the RS stress autocorrelation must be invariant under axial symmetry, i.e., verify:

$$\overset{\circ}{\underset{\approx}{C}}(r) = \mathcal{D}_M \cdot \overset{\circ}{\underset{\approx}{C}}(r) \cdot \mathcal{D}_M^T, \tag{18}$$

which constrains it to be of the form:

$$\overset{\circ}{\underset{\approx}{C}}(r) = \begin{pmatrix} C_1(r) & C_2(r) & 0 \\ C_2(r) & C_3(r) & 0 \\ 0 & 0 & C_4(r) \end{pmatrix} \tag{19}$$

with components C_i that are functions of r only. Importantly, only four of the correlation components are nonzero. In three dimensions, correlation tensors are 6×6 symmetric matrices, and invariance under axial rotations restricts them to having five nonzero components [8].

In an isotropic medium, the simple structure of the RS stress autocorrelation permits us to write, using Eq. (16), a general expression for the corresponding CS form:

$$\underset{\approx}{C}(\underline{r}) = \begin{pmatrix} C_1(r) & C_2(r)\cos 2\theta & C_2(r)\sin 2\theta \\ C_2(r)\cos 2\theta & C'(r)+C''(r)\cos 4\theta & C''(r)\sin 4\theta \\ C_2(r)\sin 2\theta & C''(r)\sin 4\theta & C'(r)-C''(r)\cos 4\theta \end{pmatrix} \tag{20}$$

with $C' = \frac{1}{2}(C_3 + C_4)$ and $C'' = \frac{1}{2}(C_3 - C_4)$. Since the C_i's are radial functions, all the angular dependencies of $\underset{\approx}{C}(\underline{r})$ appear explicitly here. They clearly correspond to those found in the CS correlation maps of Fig. 2.

The $r \to 0$ limit deserves special attention. At $r = 0$, Eq. (16) can be written for arbitrary values of direction $\hat{r}$, which amounts to requiring $\underset{\approx}{C}(0)$ to be invariant under all rotations and thus equal to $\overset{\circ}{\underset{\approx}{C}}(0)$. In view of Eq. (13), it implies that $\underset{\approx}{C}(\underline{r})$ is diagonal in the $r \to 0$ limit—local pressure and deviatoric stresses do not cross correlate—with moreover C_{22} and C_{33} being identical. Equation (20) is compatible with this requirement provided the prefactors of anisotropic terms, C_2 and C'' vanish in the $r \to 0$ limit. This condition is fully consistent with our observation in Figs. 2 and 3(a) that C_{12} and C_{13} vanish at $r = 0$, but not the functions C_1 and C', which correspond to the peaks in stress correlation maps.

D. Testing isotropy in real space

Now we use the formalism presented so far and analyze our 2D real-space correlation data. The RS autocorrelation matrix is computed from the CS data of Fig. 2 using Eq. (15). The results are reported in Fig. 4 as a matrix of pictures, each of which is centered around the origin of space, just as in Fig. 2. These fields clearly appear isotropic ($\hat{r}$ independent) in the region where data are visible, i.e., away from cell boundaries. Moreover, we do find that several fields essentially vanish, just as predicted by Eq. (19), leaving only five nonzero components.

To further characterize these data, we report in Fig. 5(a) the angle-averaged values of all the $\mathring{C}_{ab}$'s: the coefficients $\mathring{C}_{13}$ and $\mathring{C}_{23}$ that are predicted to be equal to zero by Eq. (19) are reported in thin black lines, which track perfectly the x axis, thus confirming their vanishing. The nonzero components are plotted in colors, and we clearly see that $\mathring{C}_{22}$ and $\mathring{C}_{33}$ have the same peaks but tails of opposite signs. Note that the peak of pressure fluctuations is twice as large as the peaks associated with deviatoric stress fluctuations. Also, $\mathring{C}_{12}$ does not present a peak, but vanishes at $r = 0$, as expected.

To test the quality of the expected $1/r^2$ scaling, we plot in Fig. 5(b) angle-averaged values of $r^2\mathring{C}_{ab}$ vs r, up to the boundary of the domain, $r = L/2$. It is very clear here that the pressure autocorrelation presents no long-range tail. In contrast, $r^2\mathring{C}_{22}$ and $r^2\mathring{C}_{33}$ do exhibit a flat plateau over some intermediate range, which marks the $1/r^2$ scaling; yet, they also strongly deviate from it and increase in values, starting around $r \simeq 20$, which is small compared with the half system size $L/2 = 80$, where the domain boundary lies.

The quantitative analysis of RS data runs here into a difficulty because it is not clear what causes the observed departures from scaling. They may arise, for example, from a breaking of isotropy caused by boundaries, but we will see this is not the case. Further progress will come from analyzing

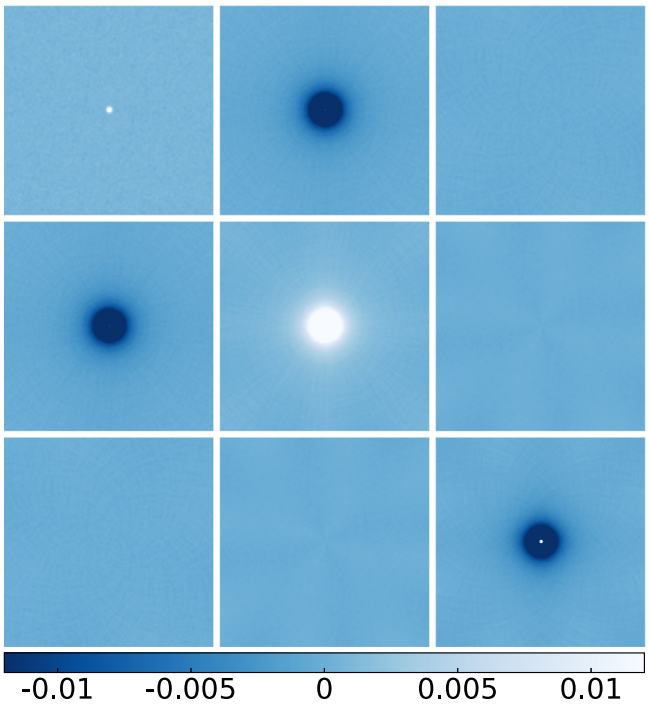

FIG. 4. The RS inherent stress autocorrelation in $L = 160$ systems, from the data of Fig. 2, using Eq. (15). The data are presented as a matrix of pictures corresponding to the fields $\mathring{C}_{ab}$ with $a,b = 1\ldots3$. In each case, the origin of space lies at the center. The color map is the same as in Fig. 2. Note that only the fields corresponding to the non-zero matrix components in Eq. (19) are visible, as predicted. The white spots at the centers of $\mathring{C}_{11}$ and $\mathring{C}_{33}$ mark the presence of positive correlation peaks.

correlations in Fourier space where important simplifications arise.

IV. STRESS AUTOCORRELATION IN FOURIER SPACE

A. Constraints and symmetries in Fourier space

1. RS and CS forms

The Fourier transform of $\underset{\approx}{C}(\underline{r})$ is the function:

$$\widehat{\underset{\approx}{C}}_{\underline{k}} = \frac{1}{A}\,\langle \widehat{\underset{\sim}{\sigma}}_{\underline{k}}\,\widehat{\underset{\sim}{\sigma}}^{*}_{\underline{k}}\rangle_c \tag{21}$$

with * the complex conjugate. For $L\times L$ periodic cells, it takes values on the discrete reciprocal space, $\underline{k} = \frac{2\pi}{L}\,\underline{n}$ with $\underline{n}\in\mathbb{Z}^2$. The RS field is defined as the autocorrelation of the corresponding radial Fourier components, i.e., as the matrix:

$$\mathring{\underset{\approx}{C}}_{\underline{k}} = \frac{1}{A}\,\langle \widehat{\underset{\sim}{\sigma}}^{\hat{\underline{k}}}_{\underline{k}}\,(\widehat{\underset{\sim}{\sigma}}^{\hat{\underline{k}}}_{\underline{k}})^{*}\rangle_c \tag{22}$$

where $\widehat{\underset{\sim}{\sigma}}^{\hat{\underline{k}}}_{\underline{k}} \equiv \mathcal{D}^{\hat{\underline{k}}}\cdot\widehat{\underset{\sim}{\sigma}}_{\underline{k}}$ is the spherical representation of tensor $\widehat{\underline{\underline{\sigma}}}_{\underline{k}}$ in frame $\mathcal{F}^{\hat{\underline{k}}}$. The relation between the CS and RS forms reads exactly the same as in real space [Eq. (15)]:

$$\mathring{\underset{\approx}{C}}_{\underline{k}} = \boldsymbol{\mathcal{D}}^{\hat{\underline{k}}}\cdot\widehat{\underset{\approx}{C}}_{\underline{k}}\cdot(\boldsymbol{\mathcal{D}}^{\hat{\underline{k}}})^{T}. \tag{23}$$

Both matrices $\mathring{\underset{\approx}{C}}_{\underline{k}}$ and $\widehat{\underset{\approx}{C}}_{\underline{k}}$ are real-valued thanks to spatial inversion symmetry.

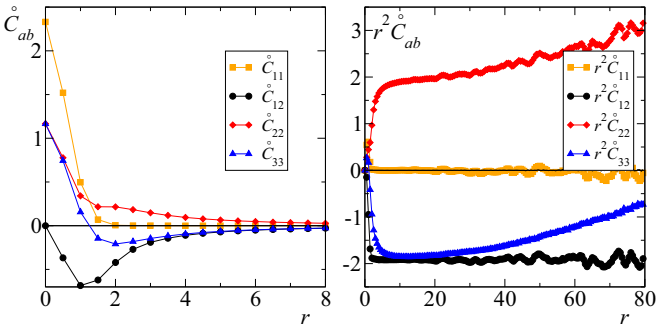

FIG. 5. Angle-averaged values of the RS correlation fields $\mathring{C}_{ab}$ in $L = 160$ systems. (a) $\mathring{C}_{ab}$ vs r. (b) $r^2\mathring{C}_{ab}$ vs r. The fields $\mathring{C}_{13}$ and $\mathring{C}_{23}$ are shown on both graphs using thin black lines: they uniformly vanish as expected from isotropy.

2. Implications of material isotropy

In an isotropic medium, $\mathring{\underset{\approx}{C}}_{\underline{k}}$ is $\hat{\underline{k}}$ independent and, since axial symmetry applies just as in real space, presents, for any nonzero $\underline{k}$, the same matrix structure as in Eq. (19):

$$\forall \underline{k}\neq\underline{0}\,,\quad \mathring{\underset{\approx}{C}}_{\underline{k}} = \begin{pmatrix} \widehat{C}_1(k) & \widehat{C}_2(k) & 0 \\ \widehat{C}_3(k) & \widehat{C}_4(k) & 0 \\ 0 & 0 & \widehat{C}_5(k) \end{pmatrix}. \tag{24}$$

Our notation emphasizes that, while $\mathring{\underset{\approx}{C}}_{\underline{k}}$ is defined at discrete $\underline{k}$'s, its values are (real) functions of the amplitude k of the wave vector only. It follows from the above expression that the corresponding Cartesian form $\widehat{\underset{\approx}{C}}_{\underline{k}}$ presents the same anisotropies as in Eq. (20).

It is important to note that, the reciprocal space being discrete, the $\underline{k} = \underline{0}$ coefficient cannot be deduced by continuity from the $\underline{k}\neq\underline{0}$ ones. As in real space, rotation invariance entails that it is of the form:

$$\widehat{\underset{\approx}{C}}_{\underline{0}} = \mathring{\underset{\approx}{C}}_{\underline{0}} = \begin{pmatrix} \widehat{C}_0 & 0 & 0 \\ 0 & \widehat{C}'_0 & 0 \\ 0 & 0 & \widehat{C}'_0 \end{pmatrix} \tag{25}$$

with $\widehat{C}_0$ and $\widehat{C}'_0$ two real numbers.

3. Implications of mechanical balance

We are interested in analyzing stress fields that are computed in ISs and hence are divergence free, i.e., verify $i\underline{k}\cdot\widehat{\underline{\underline{\sigma}}}_{\underline{k}} = \underline{0}$ (see Sec. II A 2). Denoting (k,ϕ) the polar coordinates in Fourier space, this condition is equivalent to requiring that $\widehat{\sigma}_{\underline{k}\,kk} = \widehat{\sigma}_{\underline{k}\,k\phi} = 0$ for any $\underline{k}\neq\underline{0}$. In the RS representation, it becomes:

$$\forall \underline{k}\neq\underline{0} \qquad \begin{cases} \widehat{\sigma}^{\hat{\underline{k}}}_{\underline{k}\,1} = \widehat{\sigma}^{\hat{\underline{k}}}_{\underline{k}\,2} \\ \widehat{\sigma}^{\hat{\underline{k}}}_{\underline{k}\,3} = 0 \end{cases}. \tag{26}$$

This sole condition implies that the stress autocorrelation matrix $\widehat{\underset{\approx}{C}}_{\underline{k}}$ verifies:

$$\forall \underline{k}\neq\underline{0} \qquad \mathring{\underset{\approx}{C}}_{\underline{k}} = \begin{pmatrix} \widehat{C}_{\underline{k}} & \widehat{C}_{\underline{k}} & 0 \\ \widehat{C}_{\underline{k}} & \widehat{C}_{\underline{k}} & 0 \\ 0 & 0 & 0 \end{pmatrix} \tag{27}$$

with a single, arbitrary, scalar function $\widehat{C}_{\underline{k}}$.

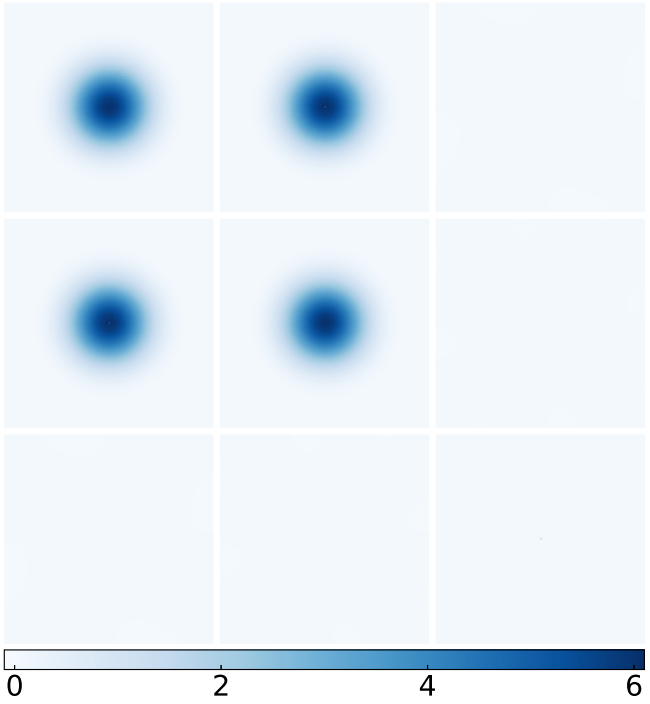

FIG. 6. The real part of $\mathring{\widehat{C}}_{\underline{k}ab}$, for the same conditions as in Figs. 2 and 4, is presented as a matrix of pictures, each of which is centered around $\underline{k} = \underline{0}$. The structure of the fields corresponds precisely to the form expected in Eq. (28).

4. Compounding mechanical balance and material isotropy

In view of Eqs. (27) and (24), if isotropy is satisfied, the inherent stress RS correlation $\mathring{\widehat{\underline{\underline{C}}}}_{\underline{k}}$ must present the following remarkably simple structure:

$$\forall \underline{k} \neq \underline{0} \quad \mathring{\widehat{\underline{\underline{C}}}}_{\underline{k}} = \begin{pmatrix} \widehat{C}(k) & \widehat{C}(k) & 0 \\ \widehat{C}(k) & \widehat{C}(k) & 0 \\ 0 & 0 & 0 \end{pmatrix} \tag{28}$$

with $\widehat{C}$ a real-valued function of k. Meanwhile, the $\underline{k} = \underline{0}$ matrix is not constrained by mechanical balance and may hence present any value consistent with Eq. (25).

The prediction that the inherent stress autocorrelation of isotropic systems should obey equation (28) is the key finding of this work. It constrains extremely tightly the spatial structure of stress correlations and will be shown in Sec. V to fix all anisotropies and long-range decays. Before we develop this argument, we check numerically that our data does abide by this form.

B. Fourier space stress autocorrelation in the RS representation

1. Data analysis at non-zero $\underline{k}$

The Fourier space RS autocorrelation matrix $\mathring{\widehat{\underline{\underline{C}}}}_{\underline{k}}$ is obtained from coarse-grained stress data by first Fourier transforming $\underline{\underline{C}}(\underline{r})$, and then applying the transformation (23). This was performed using the data of Fig. 2. As all imaginary parts vanish due to inversion symmetry, we only report on Fig. 6 the real parts of the components of $\mathring{\widehat{\underline{\underline{C}}}}_{\underline{k}}$ as a matrix of pictures centered around the origin, $\underline{k} = \underline{0}$. These data are strikingly consistent with Eq. (28) since all four components $\mathring{\widehat{C}}_{\underline{k}ab}$, with $a,b \in \{1,2\}$ look identical while all other clearly vanish.

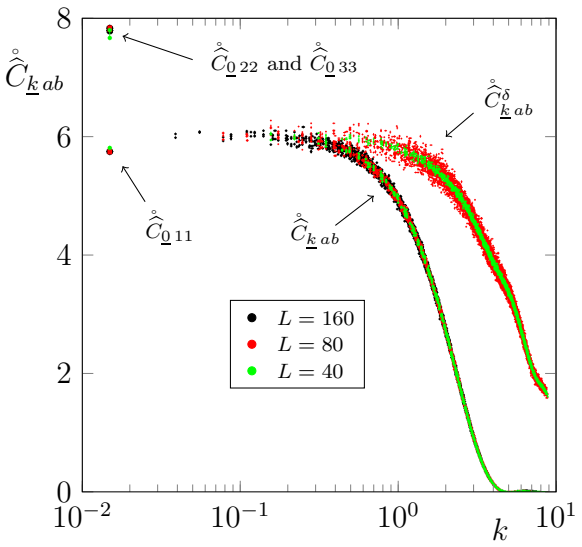

FIG. 7. Scatter plot of $\mathring{\widehat{C}}_{\underline{k}ab}$ and $\mathring{\widehat{C}}^{\delta}_{\underline{k}ab}$ vs k, for all $a,b \in \{1,2\}$, all measured $\underline{k}$ values, and different system sizes. Only $L = 40$ and $L = 80$ data are provided for $\mathring{\widehat{C}}^{\delta}_{\underline{k}ab}$ due the difficulty of its computation in large systems.

On Fig. 7 we report the most stringent possible test that our $\mathring{\widehat{\underline{\underline{C}}}}_{\underline{k}}$ data agree with Eq. (28). Namely, we construct a scatter plot, as a function of magnitude k, of all the measured $\mathring{\widehat{C}}_{\underline{k}ab}$ values, for all our $\underline{k}$'s, all $a,b \in \{1,2\}$, and using three system sizes $L = 40$, 80, and 160. The collapse of the data is absolutely remarkable. The four nonzero components of $\mathring{\widehat{\underline{\underline{C}}}}_{\underline{k}}$ are identical to each other—upon close inspection (not shown), they lie on top of each other point by point. Moreover, their values do not show any hint of dependence on the direction $\hat{\underline{k}}$. Finally, as L increases, i.e., as the set of possible k values densifies, the data points progressively fill in a single smooth master curve that identifies with $\widehat{C}(k)$.

We did not explore possible departures from collapse at smaller system sizes: our aim being to evidence residual size effects that are present in the thermodynamic limit, it is enough for our argument that our data are size independent beyond $L = 40$. This is what we imply below when referring to the absence of size effect.

A remarkable feature of these data is the total absence of finite-size deviations from collapse that, for any finite L, may have arisen at the lowest accessible $\underline{k}$'s. Indeed, the existence of a thermodynamic limit only demands that $\mathring{\widehat{\underline{\underline{C}}}}_{\underline{k}}$ achieves its $L \to \infty$ limit value above some lower cutoff $\widetilde{k}_c(L)$ that decreases with increasing L. Here, all $\mathring{\widehat{\underline{\underline{C}}}}_{\underline{k}}$ values collapse on a single curve, hence achieve their infinite medium limit values down to the lowest accessible $\underline{k}$'s at any L. We cannot explain this observation and just take it as an empirical fact.

2. $\underline{k} = \underline{0}$ values

The $\underline{k} = \underline{0}$ values of $\mathring{\widehat{\underline{\underline{C}}}}_{\underline{k}}$ are just the normalized macroscopic stress fluctuations:

$$\mathring{\widehat{\underline{\underline{C}}}}_{\underline{0}} = \widehat{\underline{\underline{C}}}_{\underline{0}} = A \, \langle \overline{\underline{\underline{\sigma}}}(t) \, \overline{\underline{\underline{\sigma}}}(t) \rangle_c \tag{29}$$

since, using translation invariance:

$$\langle \overline{\sigma}_a(t)\,\overline{\sigma}_b(t)\rangle_c = \langle \sigma_a(\underline{r}_0;t)\,\overline{\sigma}_b(t)\rangle_c = \frac{1}{A}\int_A d\underline{r}\, C_{ab}(\underline{r}) \equiv \frac{1}{A}\,\mathring{\widehat{C}}_{\underline{0}\,ab}, \tag{30}$$

where the last step was made using Eq. (1). Following the notation introduced in Eq. (25), which states that $\mathring{\underset{\approx}{\widehat{C}}}_{\underline{0}} = \underset{\approx}{\widehat{C}}_{\underline{0}}$ is diagonal in isotropic media, we denote $\widehat{C}_0 = A\langle\overline{\sigma}_1(t)\,\overline{\sigma}_1(t)\rangle_c$ and $\widehat{C}'_0 = A\langle\overline{\sigma}_2(t)\,\overline{\sigma}_2(t)\rangle_c = A\langle\overline{\sigma}_3(t)\,\overline{\sigma}_3(t)\rangle_c$. These quantities are reported on Fig. 7 using symbols positioned at an arbitrary abscissa near the y axis: they show no significant size dependence, so that macroscopic stress fluctuations scale as $1/A$.

Let us beware of our inclination to take such a law-of-large-numbers scaling as a self-evident: it usually arises because correlations vanish beyond some finite length scale, so that it is legitimate to consider a large system as a collection of independent subsystems. However, the fat tails of the stress autocorrelation rule out the validity of this assumption. For now, we also take as numerical fact that the quantities $A\,\langle\underset{\sim}{\overline{\sigma}}(t)\,\underset{\sim}{\overline{\sigma}}(t)\rangle_c$ are size independent [for $L \geqslant 40$] and will come back later to discussing why.

3. $k \to 0$ *limit*

A conspicuous feature of our $\mathring{\underset{\approx}{\widehat{C}}}_{\underline{k}}$ data is the discrepancy between the $k \to 0$ limit and the $\underline{k} = \underline{0}$ values. $\widehat{C}'_0$ is much above $\widehat{C}(0) \equiv \widehat{C}(k \to 0)$, and $\widehat{C}_0$ is slightly, but decidedly, below. Their measured values are: $\widehat{C}(0) \simeq 6.0$, $\widehat{C}_0 \simeq 5.75$, and $\widehat{C}'_0 \simeq 7.8$.

Let us emphasize that none of these three values depends on our computation method, which involves coarse graining. This is evident for $\widehat{C}_0$ and $\widehat{C}'_0$ because the spatial average of stress $\underset{\sim}{\overline{\sigma}}$ is coarse-graining independent [Eq. (6)]. However, $\widehat{C}(k)$ does depend on coarse graining. To illustrate how, we report on Fig. 7 the scatter plot of $\mathring{\underset{\approx}{\widehat{C}}}^{\delta}_{\underline{k}}$, the correlation matrix of stress fields computed in Fourier space using Eq. (5), which corresponds to the limit case $\phi = \delta^{(2)}$, the 2D δ function. The data are found again to satisfy Eq. (28) and to be size independent; they depart from our coarse-grained values at high k, but match them in the low-k limit. These features result from the definition of coarse-grained stress as $\underset{\approx}{\widehat{\sigma}}_{\underline{k}} = \widehat{\phi}(k)\,\underset{\approx}{\widehat{\sigma}}^{\delta}_{\underline{k}}$, which implies that $\mathring{\underset{\approx}{\widehat{C}}}_{\underline{k}} = |\widehat{\phi}(k)|^2\,\mathring{\underset{\approx}{\widehat{C}}}^{\delta}_{\underline{k}}$. In the low $\underline{k}$ limit, $\mathring{\underset{\approx}{\widehat{C}}}_{\underline{k}}$ and $\mathring{\underset{\approx}{\widehat{C}}}^{\delta}_{\underline{k}}$ merge because $\widehat{\phi}$ smoothly converges to $\widehat{\phi}(0) = \int \phi(\underline{r})d\underline{r} = 1$. Therefore, coarse graining only affects the high-k behavior of $\widehat{C}(k)$, which corresponds to the shape of the short-range peak, but not the $\widehat{C}(0) \equiv \widehat{C}(k \to 0)$ limit value.

V. INFINITE MEDIUM LIMIT

We showed in Sec. IV A that mechanical balance and material isotropy strongly constrain the structure of the stress autocorrelation matrix. This was expressed in Eq. (28) in terms of its Fourier RS form and confirmed to hold in our data analysis. Now, we would like to understand to what extent these two conditions determine the real-space Cartesian stress autocorrelation.

To do so, we consider the infinite medium limit, where the Fourier RS stress autocorrelation is of the form:

$$\mathring{\underset{\approx}{\widehat{C}}}^{\infty}(\underline{k}) \equiv \begin{pmatrix} \widehat{C}(k) & \widehat{C}(k) & 0 \\ \widehat{C}(k) & \widehat{C}(k) & 0 \\ 0 & 0 & 0 \end{pmatrix} \tag{31}$$

at any nonzero $\underline{k}$ in the whole plane; the smooth function $\widehat{C}(k)$ is supposed to have a finite, nonzero, $k \to 0$ limit, but is otherwise unspecified at present. Note that the $\underline{k} = \underline{0}$ value of this field, $\mathring{\underset{\approx}{\widehat{C}}}^{\infty}(0)$, obeys (25), hence cannot be the limit $\mathring{\underset{\approx}{\widehat{C}}}^{\infty}(k \to 0)$; it remains undefined and will have to be computed *a posteriori*.

The corresponding CS form is obtained by inverting Eq. (23) [i.e., performing the same transformation as from Eq. (19) to Eq. (20)]. It reads, for any $\underline{k} \neq \underline{0}$:

$$\mathring{\underset{\approx}{\widehat{C}}}^{\infty}(\underline{k}) = \begin{pmatrix} \widehat{C}(k) & \widehat{C}(k)\cos 2\phi & \widehat{C}(k)\sin 2\phi \\ \widehat{C}(k)\cos 2\phi & \frac{\widehat{C}(k)}{2} + \frac{\widehat{C}(k)}{2}\cos 4\phi & \frac{\widehat{C}(k)}{2}\sin 4\phi \\ \widehat{C}(k)\sin 2\phi & \frac{\widehat{C}(k)}{2}\sin 4\phi & \frac{\widehat{C}(k)}{2} - \frac{\widehat{C}(k)}{2}\cos 4\phi \end{pmatrix} \tag{32}$$

with ϕ the azimuth of $\underline{k}$.

The real-space CS autocorrelation is defined, on the infinite plane, as the inverse Fourier transform [Eq. (3)]:

$$\underset{\approx}{C}^{\infty}(\underline{r}) = \frac{1}{(2\pi)^2}\int d\underline{k}\, e^{i\underline{k}\cdot\underline{r}}\,\underset{\approx}{\widehat{C}}^{\infty}(\underline{k}). \tag{33}$$

We note that the $\underline{k} = \underline{0}$ value of $\underset{\approx}{\widehat{C}}^{\infty}(\underline{k})$ is irrelevant to this integral, hence does not need to be specified as yet.

The calculation proceeds noting that, for m integer:

$$\begin{aligned} &\int d\underline{k}\, e^{i\underline{k}\cdot\underline{r}}\, f(k)\cos(m\phi) \\ &\quad = 2\pi i^m \cos(m\theta)\int_0^{\infty} dk\, k f(k) J_m(kr) \\ &\int d\underline{k}\, e^{i\underline{k}\cdot\underline{r}}\, f(k)\sin(m\phi) \\ &\quad = 2\pi i^m \sin(m\theta)\int_0^{\infty} dk\, k f(k) J_m(kr) \end{aligned} \tag{34}$$

with J_m the Bessel function of the first kind of order m. Introducing the functions

$$C^{(m)}(r) \equiv \frac{1}{2\pi}\int_0^{\infty} dk\, k\,\widehat{C}(k)\,J_m(kr) \tag{35}$$

we finally obtain:

$$\underset{\approx}{C}^{\infty}(\underline{r}) = \begin{pmatrix} C^{(0)}(r) & -C^{(2)}(r)\cos 2\theta & -C^{(2)}(r)\sin 2\theta \\ -C^{(2)}(r)\cos 2\theta & \frac{C^{(0)}(r)}{2} + \frac{C^{(4)}(r)}{2}\cos 4\theta & \frac{C^{(4)}(r)}{2}\sin 4\theta \\ -C^{(2)}(r)\sin 2\theta & \frac{C^{(4)}(r)}{2}\sin 4\theta & \frac{C^{(0)}(r)}{2} - \frac{C^{(4)}(r)}{2}\cos 4\theta \end{pmatrix}, \tag{36}$$

which presents the following RS form:

$$\mathring{\underset{\approx}{C}}^{\infty}(\underline{r}) = \begin{pmatrix} C^{(0)}(r) & -C^{(2)}(r) & 0 \\ -C^{(2)}(r) & \frac{1}{2}[C^{(0)}(r)+C^{(4)}(r)] & 0 \\ 0 & 0 & \frac{1}{2}[C^{(0)}(r)-C^{(4)}(r)] \end{pmatrix}. \tag{37}$$

These two matrix fields are clearly compatible with our deductions of Sec. III C concerning the consequences of material isotropy. Note, in particular, that $C^{(2)}$ and $C^{(4)}$ vanish at $r=0$, so that $\underset{\approx}{C}^{\infty}(\underline{0}) = \mathring{\underset{\approx}{C}}^{\infty}(\underline{0})$ is diagonal with $C^{\infty}_{22}(\underline{0}) = C^{\infty}_{33}(\underline{0})$, as expected.

The function $C^{(0)}(r)$ is just $C^{\infty}_{11}(\underline{r})$, the pressure autocorrelation—and can be pictured from the measured function, $C_{11}(\underline{r}) = \mathring{C}_{11}(\underline{r})$, a cut of which was plotted on Fig. 5(a). Thus, the master curve identified in our scatter plot of Fig. 7, $\widehat{C}(k) = \widehat{C}^{\infty}_{11}(\underline{k})$, is the Fourier transform of pressure. Note also that, since $C^{(4)}$ and its first three derivatives vanish at $r=0$, all three correlation peaks are $\propto C^{(0)}(r)$. This explains the collapse seen on Fig. 5(a) of $\mathring{C}_{22}(r)$ and $\mathring{C}_{33}(r)$ near their maximum, where they reach 1/2 of the pressure peak.

Let us recall that the $\underline{k}=\underline{0}$ value of $\widehat{\underset{\approx}{C}}^{\infty}$ has so far remained unspecified. It is self-consistently defined as the $\underline{k}=\underline{0}$ Fourier transform of $\underset{\approx}{C}^{\infty}$. From Eq. (36), the θ-dependent terms integrate to zero, and it appears that:

$$\mathring{\widehat{\underset{\approx}{C}}}^{\infty}(\underline{0}) = \widehat{\underset{\approx}{C}}^{\infty}(\underline{0}) = \begin{pmatrix} \widehat{C}(0) & 0 & 0 \\ 0 & \frac{1}{2}\widehat{C}(0) & 0 \\ 0 & 0 & \frac{1}{2}\widehat{C}(0) \end{pmatrix}. \tag{38}$$

In Eq. (29), we saw that the diagonal components of $\widehat{\underset{\approx}{C}}_{\underline{0}}$ in a finite-sized system are the corresponding scaled macroscopic stress fluctuations. It will become clear in the next section that $\widehat{\underset{\approx}{C}}^{\infty}(\underline{0})$ accounts for the contribution of local inhomogeneities of pressure and deviatoric stresses to the corresponding (scaled) macroscopic stress fluctuations, $A\langle\overline{\sigma}^2_a\rangle_c$, with $a=1,2,3$. The finiteness of $\widehat{C}(0) = \int d\underline{r}\, C^{\infty}_{11}(\underline{r})$, which we observed in our Fourier data analysis, is required for this contribution to remain finite, and entails that the infinite medium pressure autocorrelation $C^{(0)}(r)$ must decay with a finite characteristic length scale.

The most striking feature of Eq. (36) is that the two functions $C^{(2)}$ and $C^{(4)}$, which set the r dependence of all anisotropic terms, are just certain transforms of $\widehat{C}$, i.e., are fully specified by the pressure autocorrelation $C^{(0)}$. Since the latter vanishes beyond a finite length, we can get the leading-order large r behavior of $C^{(2)}$ and $C^{(4)}$ by approximating $C^{\infty}_{11}(\underline{r})$ by the 2D Dirac function $\widehat{C}(0)\delta^{(2)}(\underline{r})$, which amounts to considering $\widehat{C}(k) \equiv \widehat{C}(0)$ at all k's. At leading order, we then get $C^{(m)}(r) \simeq \widehat{C}(0)\, m/(2\pi r^2)$, which not only accounts for the $1/r^2$ decay of anisotropic terms, but also implies $C^{(2)} \simeq \widehat{C}(0)/(\pi r^2) \simeq C^{(4)}/2$, so that all tails have the same amplitude, as seen on Fig. 3.

We find remarkable that all these properties now seem self-evident: in the course of previous works [7,8], we attributed the $1/r^2$ decay to elasticity. We had also observed that simple ratios existed between correlation peaks or tails, and thought that they had to be attributed to certain simplifications due to, e.g., the pairwise nature of our system. In fact, detailed features of the stress autocorrelation matrix, including anisotropy and long-range decay, are found here to originate only from the combination of isotropy and mechanical balance.

VI. FINITE-SIZE EFFECTS

A. Real-space IS stress autocorrelation in finite-sized cells

In Sec. IV B, we observed that our $\mathring{\widehat{\underset{\approx}{C}}}_{\underline{k}}$ data obtained in periodic cells were devoid of any finite-size deviation, i.e., that:

$$\begin{aligned} &\mathring{\widehat{\underset{\approx}{C}}}_{\underline{k}} = \mathring{\widehat{\underset{\approx}{C}}}^{\infty}(\underline{k}) \qquad \text{for} \quad \underline{k} \neq \underline{0} \\ &\mathring{\widehat{\underset{\approx}{C}}}_{\underline{0}} \neq \mathring{\widehat{\underset{\approx}{C}}}^{\infty}(\underline{0}) \end{aligned} \tag{39}$$

the value $\mathring{\widehat{\underset{\approx}{C}}}_{\underline{0}}$ being size independent. The same relation hence holds between the CS forms $\widehat{\underset{\approx}{C}}_{\underline{k}}$ and $\widehat{\underset{\approx}{C}}^{\infty}(\underline{k})$. Here, we use this empirical result to compute the real-space form $\underset{\approx}{C}(\underline{r})$ in finite-sized periodic cells.

Let us introduce the sum of $\underset{\approx}{C}^{\infty}$ and its images,

$$\underset{\approx}{C}^{\square}(\underline{r}) = \sum_{\underline{n}\in\mathbb{Z}^2} \underset{\approx}{C}^{\infty}(\underline{r} + L\,\underline{n}), \tag{40}$$

which is a periodic function on the $L\times L$ cell. Its Fourier coefficients are $\widehat{\underset{\approx}{C}}^{\square}_{\underline{k}} = \widehat{\underset{\approx}{C}}^{\infty}(\underline{k})$, for all $\underline{k} = 2\pi\underline{n}/L$, $\underline{n}\in\mathbb{Z}$. Using Eqs. (39), (25), and (38), we thus find:

$$\begin{aligned} &\widehat{\underset{\approx}{C}}_{\underline{k}} = \widehat{\underset{\approx}{C}}^{\square}_{\underline{k}} \qquad \text{for} \quad \underline{k} \neq \underline{0} \\ &\widehat{\underset{\approx}{C}}_{\underline{0}} = \widehat{\underset{\approx}{C}}^{\square}_{\underline{0}} + \begin{pmatrix} \delta\widehat{C}_0 & 0 & 0 \\ 0 & \delta\widehat{C}'_0 & 0 \\ 0 & 0 & \delta\widehat{C}'_0 \end{pmatrix} \end{aligned} \tag{41}$$

with

$$\begin{aligned} \delta\widehat{C}_0 &= \widehat{C}_0 - \widehat{C}(0) \\ \delta\widehat{C}'_0 &= \widehat{C}'_0 - \tfrac{1}{2}\widehat{C}(0). \end{aligned} \tag{42}$$

It follows that the real-space inherent stress autocorrelation matrix in a finite-sized periodic cell reads:

$$\underset{\approx}{C}(\underline{r}) = \underset{\approx}{C}^{\square}(\underline{r}) + \underset{\approx}{C}^{\mathrm{bg}}(\underline{r}) \tag{43}$$

with

$$\underset{\approx}{C}^{\mathrm{bg}}(\underline{r}) = \frac{1}{A}\begin{pmatrix} \delta\widehat{C}_0 & 0 & 0 \\ 0 & \delta\widehat{C}'_0 & 0 \\ 0 & 0 & \delta\widehat{C}'_0 \end{pmatrix}. \tag{44}$$

We have thus obtained for the stress autocorrelation $\underset{\approx}{C}(\underline{r})$ a complete expression that holds in finite-sized cells. It is the sum of: the infinite medium solution $\underset{\approx}{C}^{\infty}$, its periodic images, and a uniform correlation background $\underset{\approx}{C}^{\mathrm{bg}}(\underline{r})$, which is diagonal and of amplitude $\propto 1/A$.

With these elements at hand, let us return to our attempt of Sec. III D to capture in Fig. 5(b) the long-range $1/r^2$ scaling using real-space RS data. It appears at present that the growth at large distance of the angle averages of $r^2\mathring{C}_{22}(r)$ and $r^2\mathring{C}_{33}(r)$ is likely to be caused primarily by the correlation background.

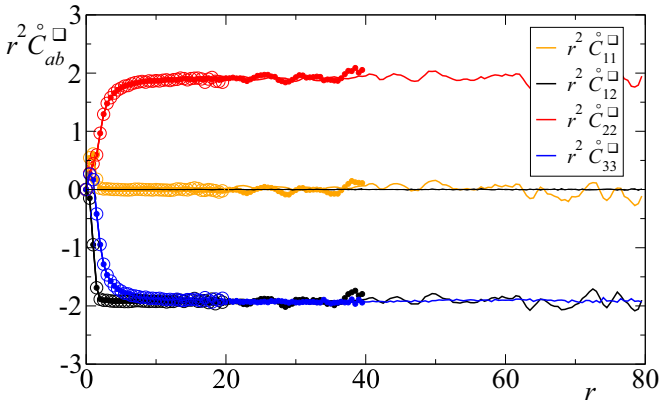

FIG. 8. $r^2\,\mathring{C}^{\square}_{ab}$ vs r, for three system sizes: $L = 40$ (open circles), 80 (filled circles), and 160 (lines).

We check this by computing $\mathring{\underset{\approx}{C}}^{\square}(r)$ using Eqs. (42), (43), and (44), with the values $\delta\widehat{C}_0 \simeq -0.25$ and $\delta\widehat{C}'_0 \simeq 4.8$, obtained from the data of Sec. IV B 3. Scaling is tested by plotting on Fig. 8 the angle-averaged values of $r^2\mathring{C}^{\square}_{ab}(r)$ vs r. We use the same colors as on Fig. 8, but now plot together our three system sizes $L = 40$, 80, and 160. The collapse onto a unique size-independent plateau is nearly perfect.

This graph provides a real-space visualization of the $1/r^2$-scaling of stress correlations. On a practical level, it shows that it is possible to access the scaling regime using our smallest system size, $L = 40$, which sanctions a tremendous simplification of the technology involved in analyzing stress correlations. Indeed, we came to use very large systems in this and previous studies because the range where it was possible to see a clear scaling was limited. We now understand that this difficulty is caused by background correlations that can be easily identified and eliminated.

B. Macroscopic stress fluctuations

The general expression we have derived for the inherent stress autocorrelation matrix, holds the key to understanding how the fluctuations of macroscopic stress are related to local stress inhomogeneities. Remember that the scaled (multiplied by A) macroscopic stress fluctuations (which are the quantities of interest in the large-size, thermodynamic limit), are just the integrals

$$A\,\langle\overline{\sigma}^2_a\rangle_c = \int_A d\underline{r}\, C_{aa}(\underline{r}). \tag{45}$$

In view of the relation $\underset{\approx}{C} = \underset{\approx}{C}^{\square} + \underset{\approx}{C}^{\rm bg}$ [Eq. (43)], all the contributions to macroscopic fluctuations other that due to the background term are captured by:

$$\int_A d\underline{r}\,\underset{\approx}{C}^{\square}(\underline{r}) = \int_{\mathbb{R}^2} d\underline{r}\,\underset{\approx}{C}^{\infty}(\underline{r}) \equiv \underset{\approx}{\widehat{C}}^{\infty}(\underline{0}) = \begin{pmatrix} \widehat{C}(0) & 0 & 0 \\ 0 & \frac{1}{2}\widehat{C}(0) & 0 \\ 0 & 0 & \frac{1}{2}\widehat{C}(0) \end{pmatrix}, \tag{46}$$

where the last equality is just Eq. (38). The first step in the above calculation, $\int_A d\underline{r}\,\underset{\approx}{C}^{\square}(\underline{r}) = \int_{\mathbb{R}^2} d\underline{r}\,\underset{\approx}{C}^{\infty}(\underline{r})$, shows that image effects do not contribute to macroscopic fluctuations. Next we have used that all long-range anisotropic terms integrate out to zero, thus showing they do not contribute either. The only nonzero contributions come from the integral $\int d\underline{r}\, C^{(0)}(r) = \widehat{C}(0)$ of the short-ranged, isotropic function $C^{(0)}(r)$.

Macroscopic stress fluctuations finally decompose into $A\,\langle\overline{\sigma}^2_a\rangle_c = \int_A d\underline{r}\, C^{\square}_{aa}(\underline{r}) + \int_A d\underline{r}\, C^{\rm bg}_{aa}(\underline{r})$, or:

$$\begin{aligned} A\,\langle\overline{\sigma}^2_1\rangle_c &= \widehat{C}(0) + \delta C_0 \\ A\,\langle\overline{\sigma}^2_2\rangle_c &= A\,\langle\overline{\sigma}^2_3\rangle_c = \tfrac{1}{2}\widehat{C}(0) + \delta C'_0, \end{aligned} \tag{47}$$

which comprise only a peak and a background term.

To interpret these expressions, it is important to have clearly in mind the classical case of an observable O that fully decorrelates beyond a finite length scale ℓ, with $C_{OO}(\underline{r}) \simeq C^{\infty}_{OO}(\underline{r})$ up to irrelevant corrections. The inverse area scaling in the large-size limit then immediately follows from

$$A\,\langle\overline{O}^2\rangle_c = \int_A d\underline{r}\, C_{OO}(\underline{r}) \to \int_{\mathbb{R}^2} d\underline{r}\, C^{\infty}_{OO}(\underline{r}). \tag{48}$$

Let us see why, in this case, spatial ergodicity holds, i.e., why $\overline{O}$ is statistically equivalent to (i.e., present the same variance as) the mean of N local averages $\overline{O}^{\rm loc}$ defined on independent, size-R, domains. The issue pertains to the $\ell \ll R \ll L$ limit, since the condition $\ell \ll R$ is required to achieve domain independence, and $R \ll L$ for the thermodynamic limit. Without loss of generality, we take as subdomains disks of radius R, and define $\overline{O}^{\rm loc}(\underline{r}) = \frac{1}{S}\int_{|\underline{r}'-\underline{r}|<R} d\underline{r}'\, O(\underline{r}')$, with $S = \pi R^2$. Introducing

$$I_{OO}(R,L) = \int_{r<R} d\underline{r}\, C_{OO}(\underline{r}) \tag{49}$$

the variance of $\overline{O}^{\rm loc}$ verifies $S\,\langle(\overline{O}^{\rm loc})^2\rangle_c \simeq I_{OO}(R,L)$, up to ℓ/R corrections, in the considered $\ell \ll R \ll L$ limit. It is key to spatial ergodicity that, in this limit, $I_{OO}(R,L)$ tends precisely to $A\,\langle\overline{O}^2\rangle_c$, so that $\langle\overline{O}^2\rangle_c \simeq \frac{S}{A}\langle(\overline{O}^{\rm loc})^2\rangle_c$: the right-hand side of this equation is indeed the variance of the mean of $N = A/S$ independent variables $\overline{O}^{\rm loc}$, and the sought-after equivalence is then established. It is in that sense that the full decorrelation of O beyond a characteristic length scale justifies viewing the macroscopic problem as equivalent to a set of independent subsystems.

To contrast this classical scenario with our situation, let us consider the integrals

$$I_{ab}(R,L) = \int_{r<R} d\underline{r}\, C_{ab}(\underline{r}), \tag{50}$$

which are taken over the intersection of the $[-L/2,L/2]^2$ square cell and the disk of radius R centered on the origin. All the functions I_{ab} are reported on Fig. 9 for a fixed $L = 160$, and for R ranging from 0 to the maximum distance $L/\sqrt{2}$, which corresponds to cell corners, where they achieve the values $I_{ab}(L/\sqrt{2},L) = A\langle\overline{\sigma}_a(t)\,\overline{\sigma}_b(t)\rangle_c$ by virtue of Eq. (30). The color convention is the same as in Figs. 5 and 8. All the I_{ab}'s associated with cross correlations ($i \neq j$, thin black lines) vanish, as expected. Only remain the three integrals I_{aa} for $a = 1,2,3$.

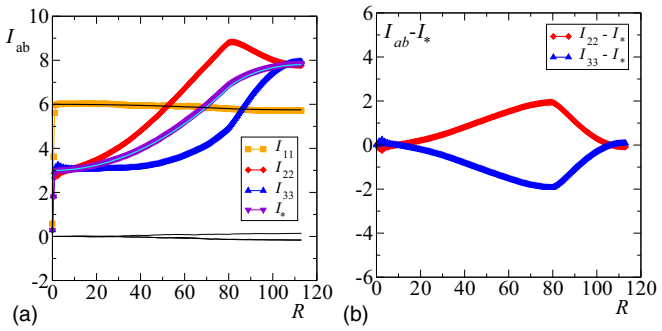

FIG. 9. (a) Integrals $I_{ab}(R)$ vs R, using the same color convention as in previous graphs. The purple line is the average $I_* = [I_{22}(R) + I_{33}(R)]/2$. The black and cyan lines tracking I_{11} and I_* (respectively), are the functions of the form $A + B\,\mathcal{A}$ as discussed in the text. (b) $I_{22} - I_*$ and $I_{33} - I_*$.

Each of these three curves presents a rapid jump near the origin, which corresponds to the integration over the peak region. Since correlation backgrounds and image superposition bring negligible contributions over such a short range, and since anisotropies do not contribute, in view of Eq. (36), the jumps for pressure and deviatoric stress correlation integrals result primarily from the integration of, respectively, $C^{(0)}$ and $\frac{1}{2}C^{(0)}$, and consistently have amplitudes $\widehat{C}(0) \simeq 6$ and $\frac{1}{2}\widehat{C}(0) \simeq 3$. As already said, these values are independent of coarse graining, which only affects the width of the central peak, i.e., the small distance over which the jump is completed.

Beyond the peak radius, I_{11}, which slightly decreases, is essentially equal to $\widehat{C}(0) + \delta C_0 \mathcal{A}/A$ (thick black line, using $\delta C_0 = -0.25$) with $\mathcal{A}$ the area of the integration domain:

$$\mathcal{A}(R,L) = \pi R^2 \quad \text{if} \quad R < L/2$$

$$\mathcal{A}(R,L) = \pi R^2 - 4R^2 \arctan\left[\sqrt{\left(\frac{2R}{L}\right)^2 - 1}\right] + L^2\sqrt{\left(\frac{2R}{L}\right)^2 - 1} \quad \text{if} \quad R > L/2. \tag{51}$$

Meanwhile, the integrals I_{22} and I_{33} display strange shapes that compel us to return to Eqs. (36), (40), and (43). We note that, since the long-ranged $\cos 4\theta$ terms—which are irrelevant to macroscopic fluctuations—have opposite signs in C_{22} and C_{33}, they and all their images cancel exactly in $C_* \equiv \frac{1}{2}[C_{22}(\underline{r}) + C_{33}(\underline{r})]$. The half sum C_* is thus essentially $\frac{1}{2}C^{(0)}(r) + \delta C_0'/A$, up to its own (negligible) periodic images; beyond the correlation peak region, its integral, $I_* = \frac{1}{2}(I_{22} + I_{33})$, reported on Fig. 9 in purple, matches nearly perfectly the equation $\frac{1}{2}\widehat{C}(0) + \delta C_0'\mathcal{A}/A$ (cyan line, using $\delta C_0' = 4.8$). The quantities $I_{22} - I_*$ and $I_{33} - I_*$, plotted on Fig. 9(b), only carry residues associated with the combined effects of anisotropy and image superposition; they are consistently in perfect symmetry with each other and vanish at the end point $R = L/\sqrt{2}$ of the integration domain. It can also be checked that, for any fixed R, these residues vanish in the $L \to \infty$ limit.

The above plots highlight that, beyond the length ℓ characterizing the decay of $C^{(0)}$, $I_{11} \simeq \widehat{C}(0) + \delta C_0 \mathcal{A}/A$ while I_{22} and I_{33} are essentially equal to $\frac{1}{2}\widehat{C}(0) + \delta C_0'\mathcal{A}/A$ up to irrelevant contributions. It ensues that, in the $\ell \ll R \ll L$ limit, the integrals I_{11} on the one hand and I_{22} and I_{33} on the other, converge, respectively, toward $\widehat{C}(0)$ and $\frac{1}{2}\widehat{C}(0)$. Moreover, in the same limit, as we previously found when discussing the classical case, the fluctuations of local stress $\overline{\sigma}^{\rm loc}$, averaged on circular domains of radius R, verify $S\langle(\widetilde{\overline{\sigma}}_a^{\rm loc})^2\rangle_c \simeq I_{aa}$, up to ℓ/R corrections. Therefore, the two quantities $\widehat{C}(0)$ and $\frac{1}{2}\widehat{C}(0)$ capture the contributions of local pressure and shear stress fluctuations to their macroscopic counterparts. This identification implies that, since correlation backgrounds bring relevant contributions in Eq. (47), the macroscopic IS stress fluctuations cannot be captured by a decomposition into subdomains. We thus conclude that ISs are not spatially ergodic.

To take the full measure of this finding, let us observe that, in the normal case, if two observables O_1 and O_2 decorrelate beyond ℓ_1 and ℓ_2 (respectively), the ratio of their macroscopic fluctuations, $\langle\overline{O}_1^2\rangle_c/\langle\overline{O}_2^2\rangle_c$, is equal to the ratio of their local fluctuations, $\langle(\overline{O}_1^{\rm loc})^2\rangle_c/\langle(\overline{O}_2^{\rm loc})^2\rangle_c$, for any splitting of the problem into R subsystems with $R \gg \max(\ell_1,\ell_2)$. Here, the ratio of local pressure to shear stress fluctuations is necessarily 2, independently of our choice of R; but, due to the background contributions in Eq. (47), macroscopic pressure fluctuations are $\simeq$30% smaller than those of deviatoric stresses. It is therefore impossible to decompose an IS into independent subsystems in such a way that stress fluctuations are consistent at both local and macroscopic scales.

VII. CONCLUSION

Let us emphasize that our work is based on the construction of a systematic framework of analysis, extending Ref. [8], that enables us to eliminate trivial anisotropies arising from tensor rotations. This development brings a number of innovations compared with prior studies. Egami has used for decades a representation of stress based on Stevens operators (which are related to real-valued spherical harmonics) [25], which is just how we decompose stress; here, we introduce RS coordinates, which are key to understanding how isotropy and mechanical balance constrain stress correlations. Furukawa *et al.* [26,27], who pioneered the study of stress-stress correlations in Fourier space (in the case of the parent stress), examined radial correlations, but not the complete correlation matrix. We hope that the present paper will motivate other groups to work using the same vocabulary and toolbox, because considerable insights can be gained from the possibility to look at the same data via both its CS vs. RS forms, and by relating Fourier fields—where tremendous simplifications occur—with their real space forms, which lend themselves more readily to interpretation.

Our key result (Sec. IV A) is that the two conditions of mechanical balance and material isotropy constrain the Fourier RS autocorrelation field into the form specified by Eqs. (28) and (25), which entails (Sec. V) that, in the infinite medium limit, the full real-space CS stress autocorrelation $\underset{\approx}{C}^{\infty}(\underline{r})$ [Eq. (36)] is fully set by the pressure autocorrelation

only. Strikingly, the expected decay of pressure correlations beyond a finite length scale in the infinite medium limit (the local character of pressure fluctuations) then mandates all anisotropic correlation components to decay as $1/r^2$. Furthermore, all correlation components are related to one another by functional transforms that set simple ratios between the relative weights of correlation peaks and tails.

The present paper thus confirms the observations of Refs. [7] and [8] of long-ranged anisotropic correlation tails in IS stress fields, yet departs from these works in showing that no reference to elasticity is needed to explain their presence. It establishes, instead, that these features hold quite generally for the local stress field of any isotropic ensemble of mechanically equilibrated configurations, which applies, in principle, to jammed systems [28]. Our work thus also explains the observations by Henkes and Chakaborty [17] of long-range anisotropic stress correlations in granular systems near jamming, without introducing any granular-specific assumption.

We were surprised in Sec. IV B to find that our Fourier data for three rather large system sizes abide by the predicted form without any measurable finite-size deviation. This empirical result enabled us to derive (Sec. VI) a general expression for $\underline{\underline{C}}(\underline{r})$ in large but finite-sized periodic cells, which revealed the presence of uniform backgrounds of amplitude $\propto 1/A$ in the autocorrelations of pressure and deviatoric stresses. On this basis, we have been able to identify precisely all microscopic contributions to macroscopic stress fluctuations and to show [Eq. (47)] that while anisotropic tails do not contribute for reasons of symmetry, a relevant contribution from correlation backgrounds is present, which respects the inverse area scaling, but breaks spatial ergodicity, i.e., the equivalence between a large IS and an ensemble of sufficiently large subsystems. It remains that we do not understand today what fixes, for example, the amplitude of these backgrounds and hence the values of macroscopic IS stress fluctuations.

Our exclusive focus on IS stress was motivated by a convergence of interests. First, ISs are important in themselves since they are the glassy solids formed from the liquid after a quench, and local stress strongly determines local elasticity, thus affecting sound propagation [9]. Second, since the relaxation process can be reduced to a series of hops between their basins of attraction, it can be characterized in principle by the consideration of changes occurring between ISs; stress increments were used to access relaxation events [7] but many questions remain. Third, the activation barriers limiting relaxation events are expectedly affected by the local IS stress or elasticity, as, e.g., events tend to occur in soft regions of space [29]; ISs inevitably control various aspects of the relaxation process and it is important to understand precisely how. We are thus convinced that the formalism introduced here and the understanding gained about the structure of IS stress correlations will prove to be useful tools in future investigations of these various topics.

Of course, in the broader context of identifying the mechanisms governing relaxation in supercooled liquids, it is crucial to eventually connect any picture we formulate in ISs to how stress relaxes in the parent liquid. A step in that direction would be to connect our work about stress (and stress increments) in ISs to space-resolved studies of the parent stress relaxation and viscosity [26,27,30–32]. This remains very challenging, however, because, as the constraints imposed upon the IS stress by mechanical balance are lifted in the parent stress, the spatial structure of its correlation is likely more complex. Also it is not clear how the correlation background identified here—or alternatively the gap between $k \to 0$ and $k = 0$ correlations—would show up in the parent liquid stress. We just note that the anomalies we found between local and macroscopic fluctuations are evocative of anomalies identified when probing how different spatial scales contribute to viscosity [26,27,30–32]: it is plausible that a connection exists between these features. Understanding to what extent long-ranged stress correlations affect static and dynamic properties of liquids and glasses is just at its beginning, but already promises to be a fascinating enterprise.

ACKNOWLEDGMENT

The author is grateful to Christiane Caroli for her comments on an early version of the manuscript.

[1] W. Kauzmann, Chem. Rev. **43**, 219 (1948).
[2] M. Goldstein, J. Chem. Phys. **51**, 3728 (1969).
[3] R. J. Speedy, Mol. Phys. **80**, 1105 (1993).
[4] F. Sciortino, W. Kob, and P. Tartaglia, Phys. Rev. Lett. **83**, 3214 (1999).
[5] S. Sastry, Nature (London) **409**, 164 (2001).
[6] A. Heuer, J. Phys.: Condens. Matter **20**, 373101 (2008).
[7] A. Lemaître, Phys. Rev. Lett. **113**, 245702 (2014).
[8] A. Lemaître, J. Chem. Phys. **143**, 164515 (2015).
[9] S. Gelin, H. Tanaka, and A. Lemaître, Nature Mater. **15**, 1177 (2016).
[10] G. Monaco and V. M. Giordano, Proc. Nat. Acad. Sci. USA **106**, 3659 (2009).
[11] G. Baldi, V. M. Giordano, and G. Monaco, Phys. Rev. B **83**, 174203 (2011).
[12] B. Ruta, G. Baldi, F. Scarponi, D. Fioretto, V. M. Giordano, and G. Monaco, J. Chem. Phys. **137**, 214502 (2012).
[13] A. Marruzzo, W. Schirmacher, A. Fratalocchi, and G. Ruocco, Sci. Rep. **3**, 1407 (2013).
[14] J. Chattoraj and A. Lemaître, Phys. Rev. Lett. **111**, 066001 (2013).
[15] K. E. Jensen, D. A. Weitz, and F. Spaepen, Phys. Rev. E **90**, 042305 (2014).
[16] B. Illing, S. Fritschi, D. Hajnal, C. Klix, P. Keim, and M. Fuchs, Phys. Rev. Lett. **117**, 208002 (2016).
[17] S. Henkes and B. Chakraborty, Phys. Rev. E **79**, 061301 (2009).
[18] V. A. Levashov, J. R. Morris, and T. Egami, Phys. Rev. Lett. **106**, 115703 (2011).
[19] B. Wu, T. Iwashita, and T. Egami, Phys. Rev. E **91**, 032301 (2015).

[20] V. A. Levashov and M. G. Stepanov, Phys. Rev. E **93**, 012602 (2016).
[21] I. Goldhirsch and C. Goldenberg, Eur. Phys. J. E **9**, 245 (2002).
[22] D. J. Evans and G. P. Morriss, *Statistical Mechanics of NonEquilibrium Liquids* (Academic Press, London, 1990).
[23] E. Bitzek, P. Koskinen, F. Gahler, M. Moseler, and P. Gumbsch, Phys. Rev. Lett. **97**, 170201 (2006).
[24] On the same machine, an IS computation by minimization with the FIRE algorithm takes about 10 min.
[25] T. Egami and D. Srolovitz, J. Phys. F **12**, 2141 (1982).
[26] A. Furukawa and H. Tanaka, Phys. Rev. Lett. **103**, 135703 (2009).
[27] A. Furukawa and H. Tanaka, Phys. Rev. E **86**, 030501 (2012).
[28] C. S. O'Hern, L. E. Silbert, A. J. Liu, and S. R. Nagel, Phys. Rev. E **68**, 011306 (2003).
[29] K. Chen, M. L. Manning, P. J. Yunker, W. G. Ellenbroek, Z. Zhang, A. J. Liu, and A. G. Yodh, Phys. Rev. Lett. **107**, 108301 (2011).
[30] T. Iwashita and T. Egami, Phys. Rev. Lett. **108**, 196001 (2012).
[31] V. A. Levashov, J. R. Morris, and T. Egami, J. Chem. Phys. **138**, 044507 (2013).
[32] V. A. Levashov, J. Chem. Phys. **141**, 124502 (2014).